

Fast Atomic-Scale Chemical Imaging of Crystalline Materials by STEM Energy-Dispersive X-ray Spectroscopy Achieved with Thin Specimens

Ping Lu^{*1}, Ren Liang Yuan² and Jian Min Zuo²

¹Sandia National Laboratories, Albuquerque, NM 87185 USA.

²Department of Materials Science and Engineering, University of Illinois at Urbana-Champaign, 1304 W Green St, Urbana, IL 61801, USA.

*Corresponding author: plu@sandia.gov

Chemical imaging at the atomic-scale by scanning transmission electron microscopy (STEM) using energy-dispersive x-ray spectroscopy (EDS) provides a powerful real-space approach to chemical characterization of crystal structures. However, applications of this powerful technique have been limited by inefficient x-ray emission and collection, which require long acquisition times (typically hundreds of seconds). Recently, using a lattice-vector translation method, we have shown that rapid atomic-scale chemical imaging using STEM-EDS can be achieved. This method provides atomic-scale chemical maps averaged over crystal areas of ~ few 10 nm² with the acquisition time of ~2 s or less. Here, we report the details of this method and, in particular, investigate the experimental conditions necessary for achieving the fast chemical mapping. It shows, in addition to usual conditions required for atomic-scale imaging, a clean and thin specimen is the essential for the technique to be successful. Phenomenological modeling shows that the localization of x-ray signals to atomic columns is a key reason. The effect of specimen thickness on the signal localization is studied by analyzing the electron probe intensity distribution within the specimen based on multislice image simulations using SrTiO₃ (STO) as a model specimen. The results of simulation show that the x-ray localization can be achieved by choosing a thin specimen, and the thickness of less than 22 nm is preferred for STO in the [001] projection for 200 keV electrons.

INTRODUCTION

Atomic-scale chemical imaging provides powerful insights into materials' structures in real space. This technique has been recently demonstrated using aberration corrected scanning transmission electron microscopy (STEM). By scanning an angstrom-sized electron probe across a thin crystalline sample oriented along a low index zone axis, atomic-scale chemical maps are obtained by collecting either electron-energy-loss spectra (EELS; thus STEM-EELS) or energy-dispersive x-ray spectra (EDS; thus STEM-EDS) (Browning et al., 1993; Kimoto et al., 2007; Muller et al., 2008; Allen et al., 2003; Allen et al., 2012; Bosman et al., 2007; Watanabe et al., 2010; Chu et al., 2010). Simultaneously, by collecting electrons which are scattered into large angles, Z-contrast or high-angle annular dark-field (HAADF) images can be obtained. The Z-contrast or HAADF image is often used as reference for locating atomic columns for the atomic-scale chemical mapping. Accompanying these experimental successes, a number of theoretical works have been dedicated to the interpretation of atomic-scale spectroscopic images (Oxley et al., 2007; D'Alfonso et al., 2010; Forbes et al., 2012).

Similar to the Z-contrast imaging, atomic-scale STEM-EDS image can be regarded as an incoherent mode of imaging (D'Alfonso et al., 2010). Using the unique chemical EDS signals, STEM-EDS can be used for the identification of atomic columns for determination of the crystal structures or phases under proper experimental conditions. The STEM-EDS atomic-scale mapping also offers several advantages over the STEM-EELS mapping including: easy image interpretation with a one-to-one correspondence between image and structure and the capability to cover more elements in the periodic table simultaneously due to a range of different x-ray peaks available. The availability of higher energy x-rays, in addition, offers the increased signal localization associated with the high energy-loss peaks. The x-ray map, therefore, is potentially more localized to the atomic-columns, providing a higher atomic-scale resolution. A number of applications have been reported recently based on STEM-EDS imaging (Lu et al., 2013; Lu et al., 2014a and 2014b), including the determination of a Fe-Co alloy structure which contains similar atomic-number atoms of Fe and Co that could not be determined by traditional imaging or diffraction techniques (*e.g.*, electron, neutron, and x-ray scattering) (Lu et al., 2014a). Nevertheless, the widespread applications of the atomic-scale EDS technique have not been realized so far.

A major shortcoming of atomic-scale STEM-EDS mapping that limits its application is that the x-ray generation and collection are still inefficient even with the best detectors currently available. To increase x-ray count rate, relatively thick TEM specimens (>70nm) have also been considered (D'Alfonso et al. 2010; Forbes et al., 2012; Allen et al., 2012). The utilization of the thick specimen, however, complicates the interpretation of atomic-scale chemical map due to dynamic electron scattering effects. The effects such as electron beam spreading, channeling and dechanneling are strongly dependent on the crystal thickness and are intense in the thick specimens. These effects can lead to so-called “cross-talk” that results in relative contribution from neighboring column even when a fine probe is focused on a specific column (Allen et al., 2012). In the practice, compensating for the poor efficiency of x-ray generation and collection is now achieved by acquiring STEM-EDS datasets as a series of image frames, where the same region is typically scanned over several hundred times in order to accumulate a high fidelity dataset. This process typically takes more than a few hundred seconds, subjecting the samples to high doses of electron irradiation. On top of this, the spatial drift-correction employed for tracking the specimen is often difficult to perform for the extended period (a few 100 s) at the atomic-scale and requires the specimen to be very stable (i.e., the drifting of specimen over a distance less than a unit cell dimension over the time period). As a result, it normally requires a number of attempts before a successful atomic-scale EDS map can be acquired. The dose and sample requirements prevent the use of the technique for any electron beam sensitive materials and also preclude the study of phase transformations and dynamics in these materials. It would be advantageous if we can extract the chemical maps from the EDS dataset obtained from a single scan or on a time-scale comparable to HAADF imaging.

In an effort of achieving rapid atomic-scale chemical imaging using STEM-EDS, we recently developed a novel method based on lattice-vector translation that consolidates the x-rays scattered over a large crystalline area into a smaller, single unit cell area (Lu et al., 2016). The fast atomic-scale mapping with an acquisition time of ~2 seconds or less was demonstrated initially using the LaAlO₃ crystal, effectively reducing the time by more than 100X. This method produces an averaged atomic-scale chemical structure from a crystalline region of few 10 nm². As a first example of the application, the technique was used to study the phase transformation in the beam-sensitive Li[Li_{0.2}Ni_{0.2}Mn_{0.6}]O₂ (LNMO) lithium ion battery cathode material. The results demonstrated the potential of the technique for time-resolved, atomic-scale investigation of

dynamic material phenomena (Lu et al., 2016). In this paper, we present the details of this technique. In particular, we further validate the technique using SrTiO₃ (STO) and investigate the experimental conditions needed for achieving fast atomic-scale mapping. We show the localization of x-ray signals to atomic columns is a critical condition for achieving fast atomic-scale mapping by phenomenological modeling. Furthermore, by analyzing the electron probe distribution in STEM geometry using multislice image simulations (Cowley, 1984), we show the effect of specimen thickness on the x-ray localization, demonstrating the advantage of using a thin specimen for atomic-scale EDS mapping, which corroborates our experimental observations.

MATERIALS AND METHODS

A FEI TitanTM G2 80-200 STEM with a Cs probe corrector and ChemiSTEMTM technology (X-FEGTM and SuperXTM EDS with four windowless silicon drift detectors) operated at 200 kV was used in this study. The EDS spectral imaging was acquired as a series of frames where the same region was scanned multiple times. An electron probe of size less than 0.13 nm, convergence angle of 18.1 mrad, and current of ~75 pA was used for data acquisition. HAADF images were recorded under similar optical conditions using an annular detector with a collection range of 60-160 mrad.

STO single-crystals in [001] orientation was used for this study. The STO TEM specimen was prepared by mechanical polishing to a thickness of less than 10 μm , followed by Ar ion milling to perforation using a Gatan Pips 691. The final ion-milling step was carried out with 2 keV Ar ions at an incidence angle of 2° to reduce surface damage. Thin specimens with a thickness of less than 20 nm were used for the experiments. The specimen thickness was estimated by EELS measurement (Williams and Carter, 1996). Elemental maps were extracted from the spectral imaging datasets with the selected EDS energy windows for each element. Background subtraction was performed following the steps previously described (Williams and Carter, 1996).

The lattice-vector translation was performed using a MATLAB script. For the STO crystal, the x-ray counts were translated into a single unit cell, and the translation was achieved by using $(a_0\vec{x}, a_0\vec{y})$ as the basic lattice translation vectors where a_0 equals 0.39 nm (*i.e.*, the lattice constant of STO) and \vec{x} and \vec{y} are the unit vectors in x - and y -directions.

Multislice image simulation was carried out using the software developed by J.M. Zuo at University of Illinois at Urbana-Champaign (Spence and Zuo, 1992). The simulation for the STO

[001] crystal used a supercell made of 10×10 unit cells (or $3.9 \text{ nm} \times 3.9 \text{ nm}$) with the sampling pixels of 512×512 . The slice thickness was half of the unit cell lattice constant or 0.195 nm .

RESULTS AND DISCUSSION

Fast Atomic-scale Chemical Imaging by Lattice-Vector Translation Method

Figure 1 illustrates schematically the lattice-vector translation method used to consolidate the x-rays scattered over a large crystal area into a smaller, single unit cell. The x-ray counts, represented by red dots, are distributed on the lattice of crystal. Due to the long-range order of the crystal lattice, there are chemically and structurally equivalent pixel positions separated by the lattice-vectors. The x-ray counts within the scanned crystal region can be translated into the equivalent positions within the unit cell as illustrated schematically in Figs.1a and 1b, leading to a statistical distribution or averaged chemical map in Fig.1c. The x-ray distribution in this illustration is statistically localized to the atomic columns (i.e., corner of the unit cell) as it can be clearly seen when the x-ray counts are concentrated in Fig.1c. The x-ray map in Fig.1c represents an averaged chemical map from the region. Alternatively, a similar map can be accomplished by using the lattice averaging method that averages x-ray count distribution within the unit cell across the scanned region (Lu et al., 2014a).

In the example shown in Fig.1, only 20 x-ray counts are used. Under our experimental conditions (particularly, a thin STO specimen of less than 20 nm), it takes less than 100 ms to produce over 20 characteristic x-ray counts, indicating this technique's potential of fast chemical mapping. In practice, due to the fact that not all x-rays are localized to atomic columns, a higher number of x-rays is needed to produce visible and statistically significant patterns. This point will be further considered in the later sections.

Figure 2 shows the experimental data obtained from a STO [001] single crystal with a crystal thickness of about 19.0 nm . STO has the perovskite crystal structure with a cubic unit cell ($a=0.39 \text{ nm}$). Its projected structure along the [001] direction is shown Fig.2a. A HAADF image from the crystal, showing the projected structure, is shown in Fig.2b. A raw x-ray count maps (200×200 pixels) of Sr (L and K combined, red-dot) and Ti (K, green-dot) extracted without the background subtraction is shown in Fig.2c, which is overlaid on the reference HAADF image used for the spectral acquisition. The spectral imaging dataset was acquired from the STO [001] by

using a 200×200 pixels frame, corresponding to physical size of $4.46 \text{ nm} \times 4.46 \text{ nm}$ ($\sim 0.022 \text{ nm/pixel}$), and was obtained after $\sim 2.0 \text{ s}$ collection, corresponding to the sum of 2 frames ($\sim 1.0 \text{ s}$ per frame with an instantaneous dwell time on each pixel of $25 \mu\text{s}$).

A total EDS spectrum summed over the region is shown in Fig.2d, showing the Sr L and Ti K peaks. The total spectrum exhibits the Sr and Ti peaks that have a high peak-to-background (P/B) ratio, typical for the TEM EDS spectrum. The total spectrum contains 409 counts of Sr (L and K) and 290 counts of Ti (K) after the background subtraction. Using the lattice-vector translation method as illustrated in Fig.1, the x-rays distributed over the region are translated into their equivalent positions within the unit cell. The statistical distributions (or averaged chemical maps) of Sr and Ti x-rays are shown in Figs. 2e and 2f. The RGB map (Fig. 2g, Sr in red, Ti in green), is obtained by combining Figs.2e and 2f and after 3-pixel moving averaging. The map clearly shows the structure of STO (Fig.2a). In this particular example, since the lattice constant of STO is known, constructing the average chemical maps (Figs.2e and 2f), are carried out by using the fixed lattice translation vectors that correspond to $m \times 17.8 \text{ pixels}$ and $n \times 17.8 \text{ pixels}$ in x - and y -directions, respectively, where m and n are integrals (from 1 to 10 for this example). The subpixel is rounded to its nearest integral in the operation, and the rounding does not produce any visible effect due to oversampling in the EDS map ($\sim 0.022 \text{ nm/pixel}$) and a relatively broad distribution x-ray counts with respect to atomic column (generally speaking, the localization is within few pixels (Lu et al., 2014b)). For an unknown crystal structure, the reference HAADF image simultaneously collected during the EDS spectral imaging can be used to determine the lattice vectors needed for the translation operation.

Fig.2h shows an EDS map which was obtained from the dataset accumulated by 4 frames or about 4 s acquisition. The longer acquisition time leads to increased overall x-ray counts (821 for Sr, 612 for Ti), further improvement in the map quality as expected. A reduction of the acquisition time to 1 s or (single frame scan) leads to a chemical map (not shown) that is noisy and difficult to recognize without the prior structural knowledge. The experimental results show fast chemical mapping can be obtained using the method described. The chemical map represents an averaged structure of a small crystalline area of about 20 nm^2 .

It is important to point out why the technique works so well given that only limited number of x-rays is available (~ 409 Sr L and K, and 290 for Ti K for acquisition time of 2 s) under the short acquisition time. One of the reason is that the characteristic EDS peaks in TEM geometry

have a high peak-to-background (P/B) ratio (as shown in the total spectrum in Fig.2d) since the background due to the bremsstrahlung radiation is generally small for the EDS peaks (>1.5 keV). Taking the Ti K peak in Fig.2d as an example, there are about 12 counts in the background and 290 counts in the Ti K peak after the background subtraction. The background, which would be difficult to be accurately removed under the short acquisition time, has a negligible effect on the map. This also points out a similar technique based on EELS would most likely not work due to high background counts associated with the EELS peaks. Other key reason is that the x-ray counts in Fig.2c are highly localized to atomic columns due to the experimental conditions we chose such that they contribute positively to the chemical map. We have found that the specimens with relatively clean surfaces and of thin thickness (less than 20 nm) are necessary for the technique to work, in addition to usual conditions typically for high-resolution STEM imaging such as a fine electron probe. Clearly, statistical localization of x-ray counts to atomic columns is a key factor for our technique to be successful, and the point is further discussed using a phenomenological model in the following section.

Effect of the Signal-to-Noise (S/N) and Signal Localization by Phenomenological Modeling

Referring to the total spectrum shown in Fig.2d, the x-ray count in the peak after the background subtraction is the signal (S). Accompanying the signal, there are also noise (N) counts due to the counting statistics. For Poisson noise, N equals to $S^{1/2}$ gives a good estimate of the noise count. The noise counts are presumably distributed randomly in the EDS raw map irrespective to the atomic columns. Among the signal counts, there are also the counts that are delocalized due to the experimental conditions such as amorphous materials on the top and/or bottom surfaces of TEM sample, and utilization of a thick specimen. The presence of native amorphous materials produces the x-rays in total spectrum (Fig.2d) that are the signals, and the distribution of those counts when unfolded in the 2-dimensional EDS map, however, is random. As a result, contribution of the x-ray signals by the amorphous materials present on TEM surfaces to the EDS map is no different from that of the noise counts. Utilization of thick specimen, on the other hand, leads to x-ray delocalization effect due to increased inelastic and thermal diffuse scattering at the higher crystal thickness.

We have developed a phenomenological model to investigate the effect of the signal-to-noise and the signal localization. Our model simulates a geometrical condition similar to our

experiments (i.e., the x-ray map of 200×200 pixels) with the lattice made of the unit cells of 18×18 pixels. The pixel-positions where x-rays reside within the 200×200 pixels map are randomly generated, and the model assumes that the map contains both the signal (S) and noise (N) counts.

To simplify the phenomenological modeling, the x-ray signals that are delocalized (whether it is due to the native amorphous materials on the specimen surfaces or the thick specimen condition) are grouped into the noise. We define the signal as counts that are localized to the respective atomic positions within a certain pixel radius (i.e., around the corner of the unit cell with a radius of R pixels in the model). The noise counts, on the other hand, are distributed randomly across the map regardless of the atomic positions. We have used $N = XS^{1/2}$ where X is greater than 1 to take into account of higher noise counts under the definition ($X=1$ corresponds to an ideal condition where the non-localization count is only due to Poisson statistics noise).

Using the above model, we have generated the x-ray maps (200×200 pixels) under various signal and noise conditions, and used the lattice-vector translation to extract the averaged count distribution (or chemical map) within the unit cell (18×18 pixels). Figures 3 shows the results of the modeling. The modeling shows that if all counts are randomly distributed (i.e., the counts are all noise), the lattice-vector translation operation cannot produce any atomic-scale map (Fig.3a). Assuming $R=6$ and $X=3$ (Figs.3b and 3c), which was estimated based on our experimental conditions (Lu et al., 2014b), a high-quality chemical map can be obtained for S of greater than 200. At S of 100, the chemical map becomes noisy and less consistent. The result of the simulation (Fig.3c) is in a qualitatively agreement with the experimental data (Fig.2).

The effect of localization plays a critical role and can be demonstrated by varying R while keeping other parameters consistent. Figure 4 shows that under same x-ray counts and S/N value, reducing the R from 6 pixels to 4 pixels or the localization radius from 0.13nm to 0.09nm substantially improve the quality of chemical map. Increasing the R from 6 pixels to 8 pixels or the radius from 0.13nm to 0.18nm, on the other hand, leads to the deleterious effect. The map becomes very noisy at S of 200 when R equals to 8.

Multislice Simulation of Electron Probe Distribution in STEM Geometry

Aside from presence of a native amorphous layer on the top and bottom surfaces of TEM sample, there are many other factors that can also lead to the delocalization of x-rays. Those factors include electron probe spreading, channeling and dechanneling, and electron thermal

scattering, and they are interdependent and strongly associated with the specimen thickness. In the following section, effect of the specimen thickness is investigated by simulating electron probe propagation under STEM condition using the multislice formulation (Spence and Zuo, 1992). This study is to understand our observation that indicates the fast atomic-scale EDS technique works the best with a thin specimen (<20nm).

There are several efforts to simulate atomic-scale chemical maps in the STEM geometry utilizing both EDS and EELS signal (Oxley et al., 2007; D'Alfonso et al., 2010; Forbes et al., 2012). No attempts are made here to repeat these works. Here, we simulate the electron probe propagation in STO [001] in the conditions specific to our experiments. By understanding electron probe distribution as a function of crystal thickness, we attempt to understand the effect of crystal thickness on x-ray localization/de-localization. We use the following ideas to comprehend the physics behind the atomic-scale EDS mapping: (1) while electron scattering within the crystal is strongly dynamic, the inelastic scattering that leads to the ionization and subsequent emission of x-rays can be considered kinematically; (2) incoherent imaging mode approximation can be used for EDS imaging similar to HAADF imaging; and (3) under the previous two considerations, for the first approximation, the EDS signal generated at a particular probe position is simply proportional to the product of integrated electron intensity along the crystal thickness and the effective ionization potentials located at respective atomic columns. The effective EDS ionization potentials have been founded to be highly localized due to availability of high energy x-rays. Previous work indicates the width (the full-widths at half-maximum) of EDS potentials is about 0.022nm for Ti (K line) and 0.033nm for Sr (L, K lines combined) (D'Alfonso et al., 2010).

Multislice formulation is a highly effective approach to simulate dynamic scattering of the electron wave-function and electron intensity distribution (Cowley, 1984). Here, only elastically scattered electrons are considered. Effects of inelastic and thermal diffuse scattering to the elastic electrons are included by using an absorption potential (Cowley, 1984). We have calculated the electron propagation along STO [001] as a function of thickness for various fixed probe positions. In Fig.5a, the probe intensity in (110) plane is shown as a function of depth for three probe positions: (1) at Ti/O column, (2) at Sr column, and (3) at the middle point between Ti/O and Sr columns along the <110> axis. The distance between the position 1 and 2 is 0.276nm and corresponds to the distance from cube-corner (Sr atom) to the face-center (O atom). The middle point between Ti/O and Sr columns (position 3) is particularly chosen here because it is the farthest

to both Sr and Ti/O columns in (110) plane in the projected structure, and in an ideal, perfectly localized situation, the probe at this position should give a little or no x-rays of Sr and Ti. The generation of the Sr and/or Ti x-rays when the probe at the position 3, therefore, is a good indicator of the delocalization effect. The electron intensity from the three probes is assigned as blue, green and red, respectively, in Fig.5a. The 3D-surface plot of the intensity is shown in Fig.5b. The color of the surface at the particular point is determined by the highest electron intensity resulted from the probe among the three positions. Fig.5c shows the intensity at the probe positions as function of the thickness for each probe. When the electron probe is on top of either Ti/O or Sr columns, the *Pendellosung* effect is strong and clearly visible. Due to the strong potential field at the columns that attracts electrons, the probe intensity is quickly concentrated into the columns (Sr, or Ti/O) and reaches a peak value at a thickness of about 3nm (2.7nm and 2.2nm to be exact for the probe at Ti/O and Sr, respectively). Afterwards, it decreases and then increases again as a result of channeling/de-channeling effect; however, overall intensity decreases due to the absorption effect (Figs.5b and 5c). The absorption due to the inelastic and thermal scattering reduces the elastic intensity at the columns and, in turn, it gives rise to the intensity of electrons that are inelastically and/or thermally scattered. The probe intensity at the Sr column decrease at a faster rate than that at the Ti/O column due to a stronger potential at the Sr columns, and has largely absorbed by a depth of the first 20nm. When the electron probe is at the middle point between Ti/O or Sr columns (position 3), the electron probe simply spreads and dissipates because there is no potential to trap the electrons. Some of the electrons, however, travel close to the columns of Ti/O and Sr (Fig.5a) at a higher crystal thickness even when the electron probe is at the position 3. These electrons contribute to ionization and subsequent generation of x-rays from the Sr and Ti atoms that are not localized to the columns in EDS map.

The effect of crystal thickness is further shown in Fig.5d, which displays the integrated intensity along the z-direction as a function of crystal thickness. At the probe position 2 or Sr column, the integrated intensity at the Sr column (solid-green-line) reaches a maximum plateau at a thick of about 30 nm. Since the integrated intensity is proportional to the x-ray production (for the first approximation), the result indicates that localized x-ray counts (Sr x-rays at Sr column) are only produced within the first 30 nm by the elastic electrons. Beyond that thickness, localized x-rays are no longer produced. At the probe position 1 or Ti/O column, the integrated intensity (solid-blue-line) continuously increases with the thickness but at a much slower rate when the

crystal thickness is greater than 30nm. This indicates the ineffectiveness of using thicker specimens to produce the localized Ti x-rays.

The disadvantage of using a thicker specimen can be further seen by looking at the integrated intensity registered at the three positions when the electron probe is at the position 3 (i.e., at the middle point between Ti/O and Sr columns). The integrated intensity (solid-red-line) at the probe position 3 when the probe is at the position 3 reaches the maximum plateau at the thickness of about 12nm, indicating nearly complete dissipation of the probe at the thickness. Few x-rays are produced at this point since the EDS potentials are not present at the position 3. The integrated intensity at the Sr (dashed-green-line) and the Ti/O (dashed-blue-line) columns when the probe is at the position 3, however, increases gradually and becomes significant at the thickness beyond 20 nm. These electrons can produce x-rays of Sr, and Ti, leading to the delocalization effect (since the probe is at the middle point between Ti/O and Sr columns).

It is important to point out that the similar thickness effects have been reported previously using image simulation by other groups (Oxley *et al.*, 2007; Forbes *et al.*, 2012). The work by Oxley *et al.* on LaMnO₃ which has the same perovskite structure, shows that the electron probe only significantly illuminates La atoms for the first 5 nm, and Mn/O atoms for the first 10nm (Oxley *et al.*, 2007). The result indicates the nonlocal nature of x-ray emission at higher crystal thicknesses due to the dynamic propagation and absorption of the probe. The thickness dependence has also been investigated by Forbes *et al.* who have included the contribution of thermally scattered electrons to atomic-scale elemental maps (Forbes *et al.*, 2012). The effect of including the thermal scattering contribution in the simulation, in general, leads to the increased contribution of x-ray emission from the off-column positions (i.e., non-localization). In particular, they show fraction of the probe that is thermally scattered increases significantly with the crystal thickness. At a crystal thickness of about 30nm and when the probe is at Ti/O and Sr columns, respectively, more than 60% and 80% of the probe has been thermally scattered. In comparison, our simulation, without including the thermally scattered electrons, represents a best case scenario. Based on Fig. 5d, using the 95% of maximum plateau value of the integrated intensity at Sr column as a threshold, we estimate a critical thickness for STO in [001] under our experimental conditions to be about 22nm. At the critical thickness the localized contribution to x-ray emission from Sr columns reaches 95% of maximum contribution. Beyond the critical thickness, generation of the localized

Sr x-ray counts becomes limited, and, on the other hand, generation of the non-localized Sr x-ray counts which is harmful for atomic-scale chemical mapping, becomes dominant.

The result of the simulation can be used to explain our experimental observations that indicate the fast atomic-scale EDS technique works well only for the thin specimen. The x-ray counts are highly localized to the atomic columns when the specimen is thin (<20nm), and these x-rays, localized to individual columns that are related by the lattice-vectors, reinforce each other by the lattice-vector translation operation, leading to a high contrast chemical maps. The thick specimen, on the other hand, although it overall produces more x-ray counts under the same experimental conditions, the additional x-ray counts that are produced beyond the thin layer (~20nm) are highly delocalized and give rise to the background that reduces the overall contrast for the map. The delocalization has a huge effect on the quality of the images which has been demonstrated by the modeling (Fig.4). The crystal thickness should be limited to less than the critical thickness in order to produce the best, highest contrast atomic-scale EDS maps per discussion.

CONCLUSIONS

We have presented the details on the fast atomic-scale chemical imaging using STEM-EDS with an acquisition time of a few seconds or less, which is achieved by utilizing the lattice-vector translation method. The novel method concentrates the x-ray counts acquired from a region of few 10 nm^2 into a single unit cell, and produces an averaged atomic-scale chemical structure for the crystalline region. The technique is further established using the STO [001] single crystal, showing the Sr and Ti chemical maps acquired with an acquisition time of about 2 s. In addition to usual requirement for atomic-scale EDS maps, the fast atomic-scale chemical imaging further requires a thin specimen (less than 20nm for STO [001]) and a specimen with the surfaces relatively free of native amorphous materials. The x-ray localization to atomic columns is critically important for achieving fast atomic-scale mapping as shown by phenomenological modeling. Multislice image simulations indicate restricting the specimen thickness below a thickness less than 22 nm is beneficial for achieving the localization for STO [001] when using 200 keV electrons.

REFERENCES

- Allen, L.J., Findlay, S. D., Lupini, A.R., Oxley, M. P. & Pennycook S.J. Atomic-resolution electron energy loss spectroscopy imaging in aberration corrected scanning transmission electron microscopy. *Phys. Rev. Lett.* **91**, 105503 (2003).
- Allen, L. J., D'Alfonso, A.J., Freitag, B., & Klenov, D. O. Chemical mapping at atomic resolution using energy-dispersive x-ray spectroscopy. *MRS Bulletin* **37**, 47-52 (2012).
- Bosman, M. *et al.* Two-dimensional mapping of chemical information at atomic resolution. *Phys. Rev. Lett.* **99**, 086102 (2007).
- Browning, N.D., Chisholm, M.F. & Pennycook, S.J. Atomic-resolution chemical analysis using a scanning transmission electron microscope. *Nature* **366**, 143 (1993).
- Chu, M.W., Liou, S.C., Chang, C.P., Choa, F.S. & Chen, C. H. Emergent chemical mapping at atomic-column resolution by energy-dispersive x-ray spectroscopy in an aberration-corrected electron microscope. *Phys. Rev. Lett.* **104**, 196101 (2010).
- Cowley, J.M. (1984). *Diffraction Physics*, 2nd edition, Elsevier Science Publishing, New York.
- D'Alfonso, A.J., Freitag, B., Klenov, V. & Allen, L.J. Atomic-resolution chemical mapping using energy-dispersive x-ray spectroscopy. *Phys. Rev.* **B 81**, 100101 (2010).
- Forbes, B.D., D'Alfonso, A.J., Williams, R.E.A., Srinivasan, R., Fraser, H.L., McComb, D.W., Freitag, B., Klenov, D.O., & Allen, L. J. Contribution of thermally scattered electrons to atomic resolution elemental maps. *Phys. Rev* **B 86**, 24108 (2012).
- Kimoto, K. *et al.* Element-selective imaging of atomic columns in a crystal using STEM and EELS. *Nature* **450**, 702 (2007).
- Lu, P., Xiong, J., Van Benthem, M, & Jia, Q.X. Atomic-scale chemical quantification of oxide interfaces using energy-dispersive X-ray spectroscopy. *App. Phys. Lett.* **102**, 173111 (2013).
- Lu, P., Zhou, L., Kramer, M.J., & Smith, D.J. Atomic-scale chemical imaging and quantification of metallic alloy structures by energy-dispersive x-ray spectroscopy. *Sci. Rep.* **4**, 3945 (2014a).
- Lu, P., Romero, E., Lee, S., MacManus-Driscoll, J. L. & Jia, Q. Chemical quantification of atomic-scale EDS maps under thin specimen conditions. *Microsc. Microanal.* **20**, 1782-1790 (2014b).

- Lu, P., Yuan, R.L., Ihlefeld, J. F., Spoerke, E.D., Pan, W., Zuo, J. M. Fast atomic-scale chemical imaging of crystalline materials and dynamic phase transformations, *Nano Letter* **16**, 2728-2733 (2016).
- Muller, D.A. *et al.* Atomic-scale chemical imaging of composition and bonding by aberration-corrected microscopy. *Science* **319**, 1073 (2008).
- Oxley, M.P., Varela, M., Pennycook, T.J., van Benthem, K., Findlay, S.D., D'Alfonso, A.J., Allen, L. J. & Pennycook, S.J. Interpreting atomic-resolution spectroscopic images. *Phys. Rev B* **76**, 064303 (2007).
- Spence J. C.H & Zuo J.M. (1992). *Electron Microdiffraction*. Plenum Press, New York.
- Watanabe, M., Kanno, M., & Okunishi, E. Atomic-resolution elemental mapping by EELS and XEDS in aberration corrected STEM. *JEOL News* **45**, 8-15 (2010).
- Williams, D.B. & Carter C. B. (1996). *Transmission electron microscopy*. Springer, New York.

ACKNOWLEDGEMENTS

Sandia National Laboratories is a multi-program laboratory managed and operated by Sandia Corporation, a wholly owned subsidiary of Lockheed Martin Corporation, for the US Department of Energy's National Nuclear Security Administration under contract DE-AC04-94AL85000.

FIGURE CAPTIONS

Figure 1. Schematics showing the lattice-vector translation method used for consolidating x-rays: (a) x-rays (represented by red-dots) distributed over a crystal region made of approximately 4×4 unit cells; (b) the translation of two x-rays (marked by 1 and 2) to their equivalent positions within the unit cell; and (c) formation of a chemical map after all 20 x-rays are translated.

Figure 2. Fast STEM-EDS atomic-scale chemical mapping demonstrated with a STO crystal: (a) projected STO structure in [001] direction; (b) a HAADF image of STO [001]; (b) raw x-ray count maps of Sr L and K (red-dot) and Ti K (green-dot), obtained by STEM EDS with a total acquisition of ~ 2 s, overlaid on the reference HAADF image; (d) summed EDS spectrum from the region; (e, f) x-ray count maps (2×2 unit cells shown) for Sr L and K, and Ti K x-rays, respectively, obtained by the lattice-vector translation method using the x-ray map in (c); (g) RGB map (Sr L and K in red, Ti K in green) obtained by 3-point smoothing of the maps in (e, f); (h) RGB map obtained with a total acquisition of ~ 4 s. The dashed square in (a, b, c, e, f, g and h) represents the projected STO unit cell in [001] projection.

Figure 3. Chemical maps (2×2 unit cells shown) extracted by the lattice-vector translation method using the x-ray count maps simulated by the phenomenological model under various signal (S) and noise (N) conditions. The S and N values are marked for each image. In (a), x-ray counts are all noise; in (b) $R=6$ and $X=3$ are used; (c) obtained by 3-point smoothing of the maps in (b). The dashed squares represent the unit cell.

Figure 4. Chemical maps (2×2 unit cells shown) extracted by the lattice-vector translation method using the x-ray count maps simulated by the phenomenological model for S of 200 and N of 42 under three localizations conditions: (a) $R=4$; (b) $R=6$; and (c) $R=8$. The top panels are the count maps, and the bottom panels are obtained by 3-point smoothing of the maps in the top panels. The dashed squares represent the unit cell.

Figure 5. Electron probe propagation in STO [001] for three specific probe positions simulated by the multislice formulation. (a) the probe intensity distribution in (110) plane (blue – for probe at

the position 1; green – for probe at the position 2; and red – for probe at the position 3); (b) the surface plot of (a) showing the variation of intensity when probes are at three positions; (c) the electron intensities at three positions (1, 2, and 3) as function of crystal thickness when the probes are at the positions, respectively; (d) the integrated-intensities about the thickness (z) as function of crystal thickness at three positions (1, 2, and 3) when the probes are at the three positions, respectively, as well as the intensity registered at the probe positions (1, 2) due to the probe at position 3 (dashed-lines). The line-profiles in (c, d) are averaged over a radius of 0.015 nm in (001) plane about the positions.

FIGURES

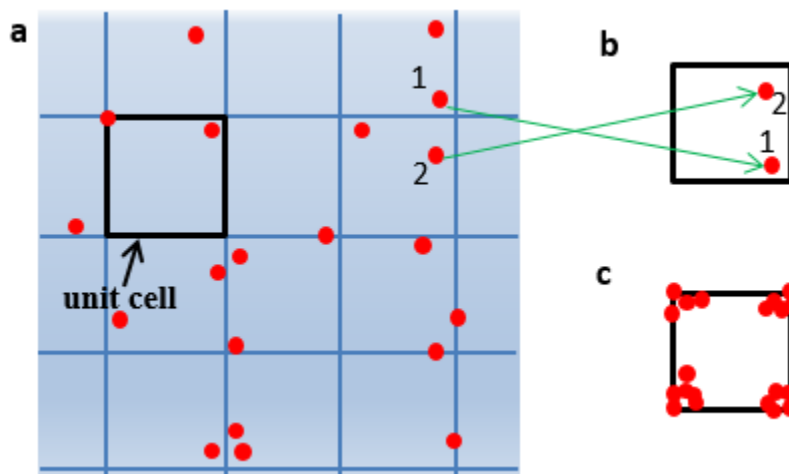


Figure 1. Schematic showing the lattice-vector translation method used for consolidating x-rays: (a) x-rays (represented by red-dots) distributed over a crystal region made of roughly 4×4 unit cells; (b) the translation of two x-rays (marked by 1 and 2) to their equivalent positions within the unit cell; and (c) formation of a chemical map after all 20 x-rays are translated.

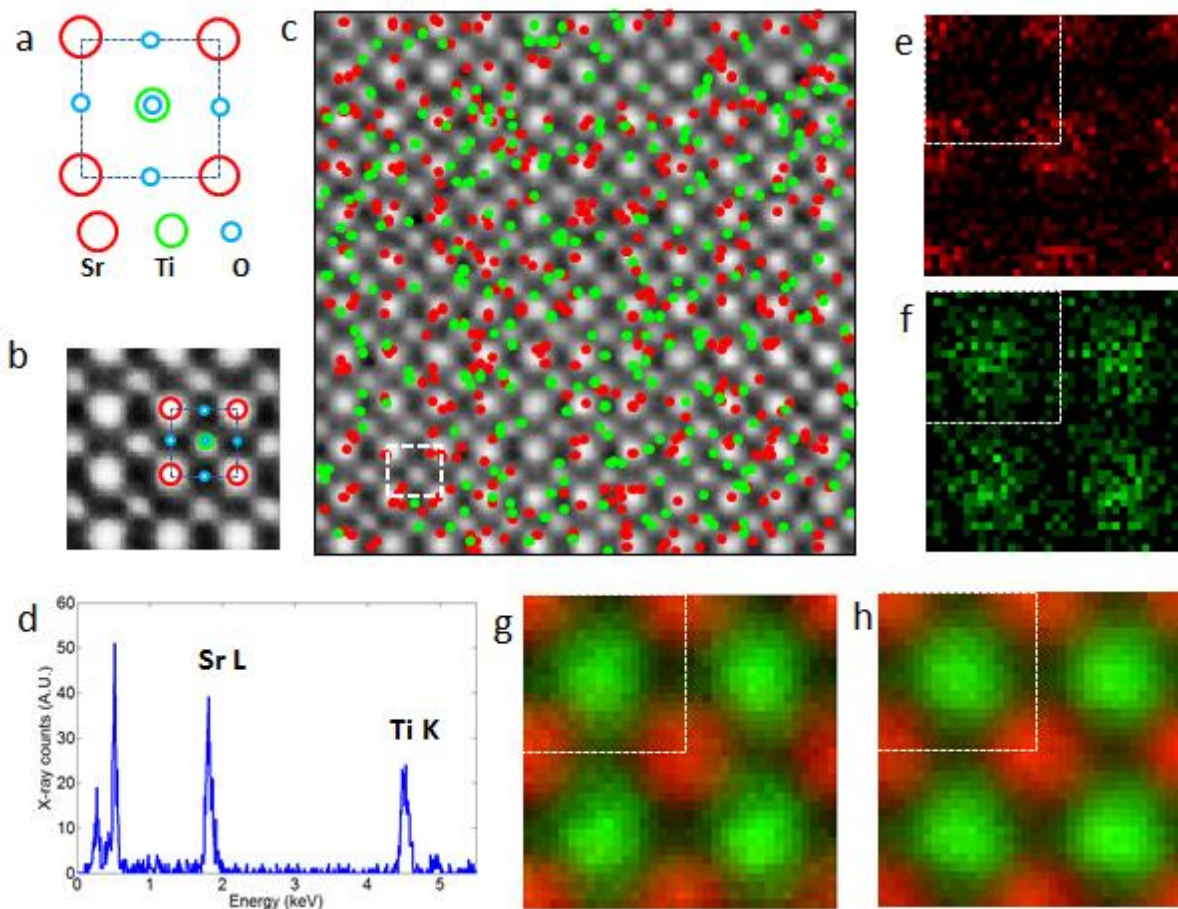


Figure 2. Fast STEM-EDS atomic-scale chemical mapping demonstrated with a STO crystal: (a) projected STO structure in [001] direction; (b) a HAADF image of STO [001]; (b) raw x-ray count maps of Sr L and K (red-dot) and Ti K (green-dot), obtained by STEM EDS with a total acquisition of ~ 2 s, overlaid on the reference HAADF image; (d) summed EDS spectrum from the region; (e, f) x-ray count maps (2×2 unit cells shown) for Sr L and K, and Ti K x-rays, respectively, obtained by the lattice-vector translation method using the x-ray map in (c); (g) RGB map (Sr L and K in red, Ti K in green) obtained by 3-point smoothing of the maps in (e, f); (h) RGB map obtained with a total acquisition of ~ 4 s. The dashed square in (a, b, c, e, f, g and h) represents the projected STO unit cell in [001] projection.

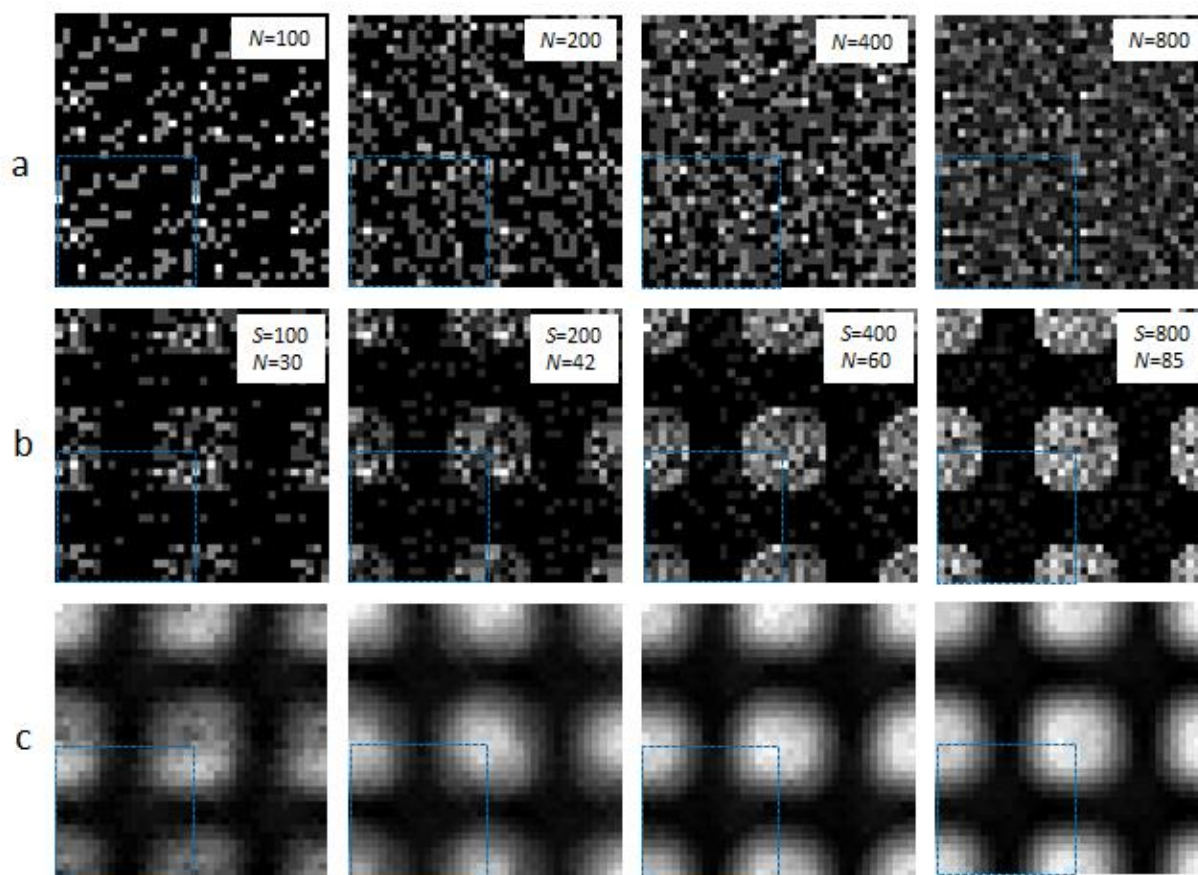


Figure 3. Chemical maps (2×2 unit cells shown) extracted by the lattice-vector translation method using the x-ray count maps simulated by the phenomenological model under various signal (S) and noise (N) conditions. The S and N values are marked for each image. In (a), x-ray counts are all noise; in (b) $R=6$ and $X=3$ are used; (c) obtained by 3-point smoothing of the maps in (b). The dashed squares represent the unit cell.

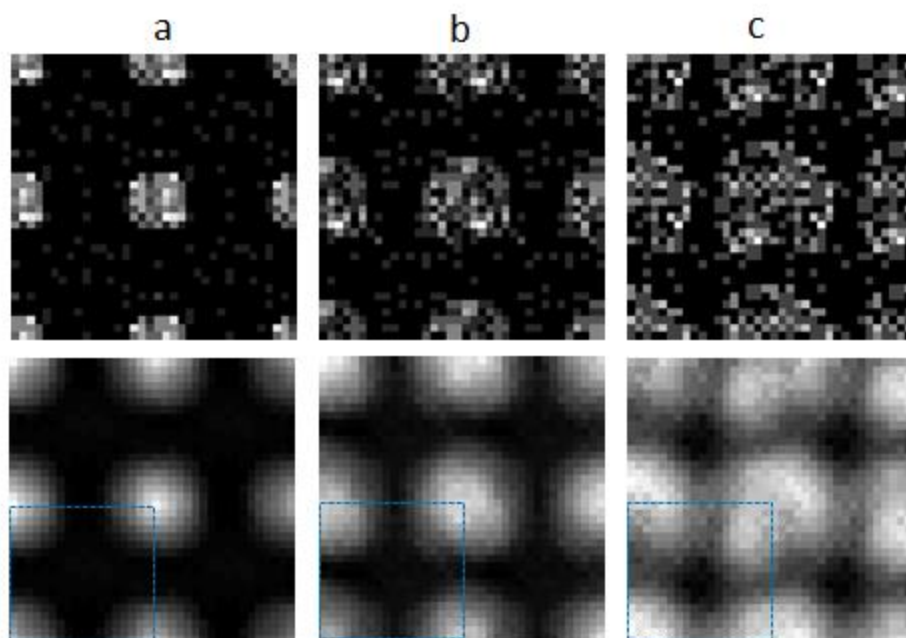


Figure 4. Chemical maps (2×2 unit cells shown) extracted by the lattice-vector translation method using the x-ray count maps simulated by the phenomenological model for S of 200 and N of 42 under three localizations conditions: (a) $R=4$; (b) $R=6$; and (c) $R=8$. The top panels are the count maps, and the bottom panels are obtained by 3-point smoothing of the maps in the top panels. The dashed squares represent the unit cell.

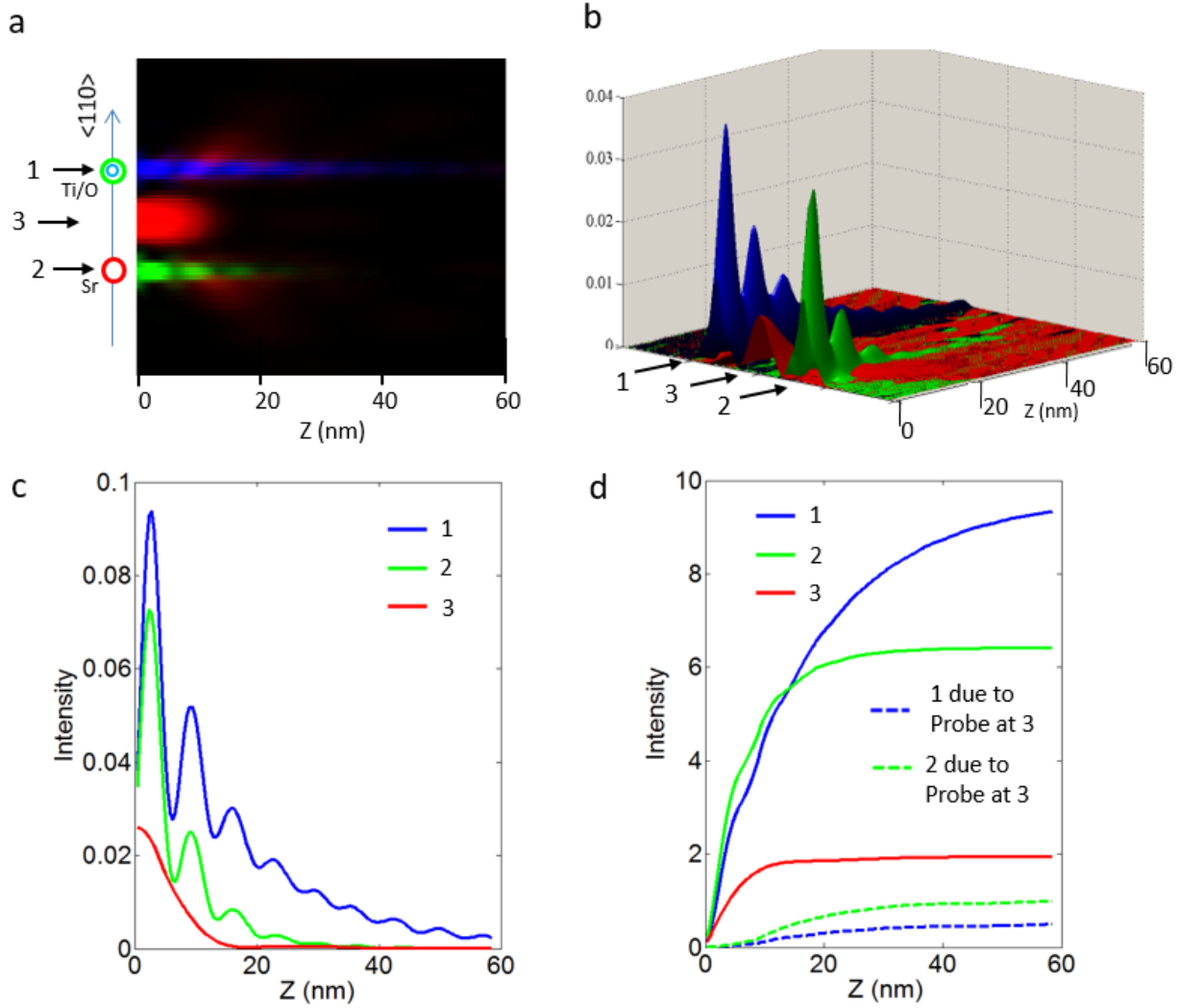


Figure 5. Electron probe propagation in STO [001] for three specific probe positions simulated by the multislice formulation. (a) the probe intensity distribution in (110) plane (blue – for probe at the position 1; green – for probe at the position 2; and red – for probe at the position 3); (b) the surface plot of (a) showing the variation of intensity when probes are at three positions; (c) the electron intensities at three positions (1, 2, and 3) as function of crystal thickness when the probes are at the positions, respectively; (d) the integrated-intensities about the thickness (z) as function of crystal thickness at three positions (1, 2, and 3) when the probes are at the three positions, respectively, as well as the intensity registered at the probe positions (1, 2) due to the probe at position 3 (dashed-lines). The line-profiles in (c, d) are averaged over a radius of 0.015 nm in (001) plane about the positions.